

Interfacial Oxide Modulated unique Exchange Bias in CrPS₄/Fe₃GeTe₂ van der Waals heterostructures

Aravind Puthirath Balan^{1‡*}, Aditya Kumar^{1‡}, Tanja Scholz², Zhongchong Lin³, Aga Shahee^{1†}, Shuai Fu⁴, Thibaud Denneulin⁵, András Kovács⁵, Rafal E. Dunin-Borkowski⁵, Hai I. Wang⁴, Jinbo Yang³, Bettina Lotsch², Ulrich Nowak⁶, Mathias Kläui^{1,7*}

¹Institute of Physics, Johannes Gutenberg University Mainz, Staudinger Weg 7, 55128 Mainz, Germany.

²Max Planck Institute for Solid State Research, Stuttgart, Germany.

³State Key Laboratory for Artificial Microstructure and Mesoscopic Physics, School of Physics, Peking University, Beijing 100871, China.

⁴Max Planck Institute for Polymer Research Mainz, Germany

⁵Ernst Ruska-Centre for Microscopy and Spectroscopy with Electrons and Peter Grünberg Institute, Forschungszentrum Jülich, 52425 Jülich, Germany

⁶Department of Physics, University of Konstanz, Germany

⁷Centre for Quantum Spintronics, Department of Physics, Norwegian University of Science and Technology, 7491 Trondheim, Norway.

[‡]These authors contributed equally

* Correspondence to aravindputhirath@uni-mainz.de, klaeui@uni-mainz.de

Abstract

Two-dimensional van der Waals heterostructures are an attractive platform for studying exchange bias due to their defect free and atomically flat interfaces. Chromium thiophosphate (CrPS_4), an antiferromagnet, has uncompensated magnetic spins in a single layer that make it an excellent candidate for studying exchange bias. In this study, we examined the exchange bias in $\text{CrPS}_4/\text{Fe}_3\text{GeTe}_2$ van der Waals heterostructures using anomalous Hall measurements. Our results show that the exchange bias strength is robust for clean interfaces, with a hysteresis loop shift of about 55 mT at 5 K for few-layer Fe_3GeTe_2 , which is larger than that obtained in most van der Waals AFM/FM heterostructures. However, when exposed to air, the ferromagnetic Fe_3GeTe_2 layer develops a thin surface oxide layer that significantly modulates the exchange bias. Remarkably, this surface oxide layer can induce exchange bias without any field-cooling, but merely by applying a 'preset field' from 5 K up to 140K due to the presence of ferrimagnetic magnetite. We also observed exchange bias beyond the Néel temperature of CrPS_4 , with two local minima due to contributions from CrPS_4 and surface oxides. These results illustrate the complex behaviour of exchange bias in van der Waals heterostructures and its potential for tailored control.

KEYWORDS: vdW magnetic materials, exchange bias, vdW heterostructures

Introduction

Exchange bias (EB) is the generation of a unidirectional magnetic anisotropy when a ferromagnet (FM) and an antiferromagnet (AFM) are brought in contact to form an interface [1]. This unidirectional anisotropy thus introduced by the proximity of a native AFM results in a shift of the magnetic hysteresis loop of the FM along the field axis. EB is an integral part of various device technologies, such as spin valves, which are extensively used in high-density magnetic storage and

sensor applications [2]. It is widely accepted that the underlying reason for EB is the exchange coupling of uncompensated spins of the AFM with the FM moments across the interface [3-4]. Although EB is, hence, generally considered as a purely interfacial phenomenon, there is compelling evidence that the precise magnetic state of the AFM at the interface is also affected by the AFM bulk which in turn is the origin of the observed EB [3]. However, in thin-film heterostructures, often consisting of layers of non-van der Waals solids, the interfaces may not be ideal for understanding precisely the origin of EB, because the interface is contaminated by several imperfections, such as interdiffusion, step edges, grain-boundaries, interfacial stress, and roughness [5].

The recent discoveries of van der Waals (vdW) magnetic materials with atomically flat surfaces has revived interest in investigation and understanding the microscopic origin of EB [6]. Owing to their inherent layered nature, vdW materials are capable of forming heterostructures with close-to-ideal interfaces, which makes them exciting for studying interface-related effects, especially for EB [7]. Recently first reports of EB in vdW FM/AFM heterostructures have been published. An EB of about 50 mT was reported in a $\text{CrCl}_3/\text{Fe}_3\text{GeTe}_2$ heterostructure at 2.5 K [8]. Follow-up reports involved different types of vdW AFM layers (MnPS_3 , MnPSe_3 , FePS_3) on either metallic Fe_3GeTe_2 or Fe_5GeTe_2 [9], [10]. Significant EB was observed on a heterostructure composed of a vdW FM insulator and an antiferromagnetic topological insulator ($\text{CrI}_3/\text{MnBi}_2\text{Te}_4$) [11]. EB observed in natural superlattice structures of $\text{MnBi}_2\text{Te}_4(\text{Bi}_2\text{Te}_3)_n$ ($n = 1, 2$) is one of the latest developments due to the exchange coupling between co-existing ferromagnetic and antiferromagnetic components in the ground state [12].

Among the available vdW antiferromagnetic materials, CrPS_4 (CPS) has several advantages of being air-stable, having an intralayer ferromagnetic coupling, and accessible spin-

flop and spin-flip transitions [13]. In particular, for the investigation of EB, a fully uncompensated layer forming the interface would be a perfect choice. While the properties of CPS have been recently studied [14], investigation of EB in vdW heterostructures involving CPS as the antiferromagnetic layer has not been reported. Moreover, Fe_3GeTe_2 (FGT) is an itinerant vdW ferromagnet, which is air-sensitive and readily forms a thin surface oxide layer upon exposure to ambient air. Recent reports have claimed that the surface oxide layer is antiferromagnetically coupled to the underlying crystal and contributes to induce EB in few layers of FGT and enhances EB in FGT/CrOCl heterostructures [15-19]. However, no studies have elucidated the nature of the formed oxide layer and how it contributes to introduction or modulation of EB.

In this study, we analyze the properties of exchange bias (EB) in vdW heterostructures comprising CPS and FGT, using transport measurements. Our findings reveal that these heterostructures exhibit a robust intrinsic EB at their interfaces. Additionally, we observe that the formation of oxide layer at the interface of exposed heterostructures can generate and alter the EB. By examining both the intrinsic EB and the EB induced and modified by the oxide layer, we establish a pathway to tailor the total EB of the CPS/FGT vdW heterostructures.

Materials and Methods

a) Sample Fabrication and analysis

Bulk single crystal FGT and CPS were grown by chemical vapour transport. The crystals were characterised using Raman Spectroscopy. FGT and CPS single crystals were mechanically exfoliated on to a clean Si/SiO₂ (300 nm) substrate using a scotch tape inside the glovebox equipped with argon inert atmosphere with O₂ and H₂O less than 0.5 ppm. Suitable FGT flakes were dry transferred by a 2D dry transfer station inside the glovebox on to a pre-patterned Hall contacts of 25/5 nm Au/Cr fabricated by standard e-beam lithography. Afterward, two devices were fabricated by transferring CPS flakes with flat bottoms that come in contact with a clean FGT

surface and another one with a thin oxide layer on top using a 2D dry transfer station. The oxide layer was formed on the FGT flake by exposing it in ambient air for about 30 minutes before stamping CPS flake on top. The Oxide layer formation was confirmed using cross-sectional transmission electron microscope (TEM) measurements (please refer *Supporting Information Section 1* for details). The device with a clean interface was further encapsulated with hexagonal boron nitride inside the glovebox before taking it out to elude any further chances of oxidation. The thickness of the FGT and CPS of the exposed heterostructure was determined using Veeco 3100 Dimension Atomic Force Microscope (Bruker). These devices were used for transport measurements.

b) Transport measurements

The electrical transport measurements were done in liquid helium cryostat with VTI and field precision of ~ 0.1 mT and max field of 12 T. Applied current density was $\sim 6.7 \times 10^6 \text{ Am}^{-2}$ for a 1 μA current and the current was transmitted through the FGT flake along x-direction and the anomalous Hall voltage (V_{xy}) was measured across the transverse terminals along y-direction. The cooling and sweeping fields were both applied in OOP orientation. Keithley 2400 source meter was used to flow current through the device, and Keithley 2182a nanovoltmeter was used to measure voltage.

Results and Discussions

Single crystals of FGT and CPS were grown using chemical vapour transport following previous reports [20], [21]. The quality of synthesized crystals was examined by Raman spectroscopy (*Figure 1a-b*). All the modes obtained for both FGT and CPS bulk crystals match well with predicted Raman modes [22-23]. Few layered flakes were exfoliated onto Si/SiO₂ (300 nm) substrates using standard mechanical exfoliation using scotch tape. Suitable flakes of uniform

thickness were located using an optical microscope. The located FGT and CPS flakes were picked up and transferred in the order mentioned to pre-patterned Hall contacts of Au/Cr (25 nm/5 nm) on Si/SiO₂ (300 nm) fabricated employing standard e-beam lithography. The resulting CPS/FGT heterostructure was then encapsulated by hexagonal boron nitride (h-BN) flakes to prevent oxidation in air. The entire process was carried out inside a glovebox containing an inert atmosphere (argon gas), and oxygen and moisture levels were kept below 0.5 ppm. This makes the CPS/FGT interface clean without any adsorbed impurities. In order to study the effect of the surface oxide formed at the FM/AFM interface on EB, new devices were fabricated following a strategy similar to that discussed above. However, the surface of FGT was exposed to the ambient atmosphere for about 30 minutes before transferring the CPS layer. The thickness of the FM and AFM layers of the exposed heterostructure was determined to be 30 nm and 100 nm, respectively, using atomic force microscope (please refer to *Figure S1* in *Section 2*). The surface oxide formation was confirmed using element-sensitive cross-sectional transmission electron microscopy measurements of an exposed FGT flake capped with platinum (Pt) (*Figure 1c-e*). Both devices with clean and exposed interfaces were then wire-bonded and immediately loaded onto a variable temperature insert (VTI) cryostat in which we can apply a magnetic field up to 12 T for anomalous Hall effect (AHE) measurements. Since CPS is an insulating antiferromagnet, the current will only flow through the metallic FGT layer. We estimate the thickness of the FGT flake with a clean interface is comparable to the thickness (30 nm) of FGT flake in the exposed device from the optical contrast of the flakes. The cross-section area of the current channel (10 μm x 5 μm) is $1.5 \times 10^{-13} \text{ m}^2$, and is used to calculate the current density, which is approximately $6.7 \times 10^6 \text{ Am}^{-2}$ for an applied current of 1 μA .

To analyse the EB, the first device with a clean interface (see *Figure 2c* inset for the optical image) was field-cooled from room temperature to below the Néel temperature of CPS ($T_N = 36$ K) with an out of the plane field of 8 T. After the field cooling, AHE measurements were carried out at various temperatures with an applied DC current along the x-direction at a current density of $6.7 \times 10^6 \text{ Am}^{-2}$. The transverse voltage (V_{xy}) was plotted as a function of the sweeping field, the maximum value of which was sufficient enough to saturate the ferromagnet. Measurements were done at various temperatures from 5 K to 50 K in steps of 5 K for both +8 T and -8 T field cooling. T-dependent (for 5 K, 15 K and 30 K) V_{xy} is then plotted as a function of the applied field for both +8 T and -8 T field cooling in *Figure 2a* and *Figure 2b*, respectively. The entire measurements at various temperatures from 5 to 50 K for both +8 T and -8 T field-cooling are depicted in *Figure S2* in *Section 3*. The EB was plotted as a function of temperature for both +8 T and -8 T field cooling (*Figure 2c*). At 5 K, the magnitude of EB is found to be ~ 55 mT for both positive and negative field cooling, and gradually decreases with increase in temperature: it becomes < 20 mT above 20 K and negligible above the Néel temperature of CPS (36 K) with error bars of ± 5 mT. The polarity of EB is negative since the loop shifts in the opposite direction of the cooling field (H_{CF}).

For the second device with the surface oxide on FGT, however, the EB follows a complex non-monotonic trend with the temperature, as depicted in *Figure 3d*. Interestingly, large EB was observed even above the Néel temperature of CPS (36 K). This surprising finding can be explained taking into the surface oxide formed on the FGT layer. Such an oxide layer formation was previously reported [15-19]. EB was measured following a +8 T field cooling from room temperature at various temperatures from 5 K to 150 K and plotted as a function of temperature along the x-axis. As indicated by green circles in *Figure 3d*, the observed trend consists of three

distinct regions (colour coded) consisting of two local minima at ~ 20 K and ~ 70 K, respectively. *Figure 3a* demonstrates representative field sweeps from all three regions for +8 T field cooling (refer to *Figure S3c* in *Section 4* for the plots at all different temperatures).

The reduced value of $|H_{EB}|$ and sharp decrease to a minimum of about 20 K are corresponding to the blocking temperature (T_B) of CPS [20]. Moreover, the effective field of the saturated FGT layer at 20 K (~ 6.5 T) [13] may just be sufficient to keep the CPS be in its spin-flip state to become FM even after the removal of the cooling field. The CPS layer retains its spin-flip FM state up to $T_N = 36$ K where it becomes paramagnetic. Above 20 K, CPS in a spin-flip FM state, reduces the EB due to the oxide layer, the effect of which becomes weaker and weaker as the temperature approaches T_N . This explains why the EB slightly increases from 20 K to 36 K. Above 36 K, only the oxide layer contributes to the EB. The second minimum at 70 K further suggests that two different phases in the surface oxide contribute to EB. Another important observation is that the oxide layer can induce EB even without field-cooling by merely applying a pre-set field (H_{PF}), and the EB due to ± 1 T pre-set field follows a similar trend as obtained for field-cooling. Representative field sweeps from three regions for both +1 T and -1 T pre-set fields are provided in *Figure 3b* and *Figure 3c*, respectively (refer to *Figure S3a & S3b* in *Section 4* for the plots at all different temperatures). This suggests that one of the oxide phases could be ferrimagnetic Fe_3O_4 , aligning, which can set the direction of unidirectional exchange anisotropy [24]. This is also confirmed by the observation of a sudden jump in longitudinal resistance of an oxidized FGT flake at about 125K, a characteristic of Verwey transition in Fe_3O_4 (Refer to *Figure S4a* in *Section 5*). At a particular temperature, the minimum field required to saturate the ferrimagnetic Fe_3O_4 is equivalent to the critical pre-set field (H_{CF}) for the system. This allowed us to judiciously choose the direction of EB by applying a pre-set field greater than the critical pre-

set field in the required direction. Sweeping the field with a maximum value greater than the critical pre-set field at a given temperature results in zero EB (please refer to *Figure S5a-d* in *Section 6*) since there is no preferred pinning by Ferrimagnetic Fe_3O_4 [25]. The second oxide phase could be ultra-thin antiferromagnetic FeO , which was reported to have a very low blocking temperature, T_B of ~ 70 K, well lower than the bulk Néel temperature ($T_N = 198\text{K}$) [26]. Above 70K, EB is due to ferrimagnetic Fe_3O_4 , which disappears at 140K, the blocking temperature.

Finally, the complex trend of EB with respect to the temperature could be understood based on an intuitive model of the contributions of CPS as well as the two phases in the surface oxide layer. The intuitive model is schematically represented in *Figure 4*. The various magnetic layers are colour coded. The blue and yellow layers are the bottom and top layers of CPS and FGT on either side of the van der Waals gap, whereas the red and magenta colours denote Fe_3O_4 and FeO phases in the surface oxide. In the case of the first device with a clean interface, field-cooling below the Néel temperature of CPS (36 K) will induce uniaxial exchange-anisotropy by direct ferromagnetic coupling of CPS moments with FGT moments across the van der Waals gap (*Figure 4a*). In the case of the second device with the surface oxide, however, three cases have to be considered: (i) $T < 36$ K (*Figure 4b*), where all the three magnetic layers are magnetically ordered, (ii) $36 \text{ K} < T < 70 \text{ K}$ (*Figure 4c*), where CPS is paramagnetic, while both oxide phases are antiferromagnetic, and (iii) $70 \text{ K} < T < 140 \text{ K}$ (*Figure 4d*), where Fe_3O_4 and FeO layers are magnetically ordered, however, only Fe_3O_4 contributes to EB since T_B of FeO is at 70 K. In the first case, since all the magnetic layers are in their magnetically ordered state, the resulting EB is then the net effect of all three EB contributions. The first local minimum of about ~ 20 K could be the T_B of CPS. Additionally, above 20 K, the CPS would be in its spin-flip FM state due to the effective exchange field of saturated FGT, the strength of which gradually decreases as the

temperature increases and becomes paramagnetic above 36 K, the Néel temperature of CPS. This contributes to a slight increase of $|H_{EB}|$ from the minimum at 20 K to 36 K. In the second case, CPS is paramagnetic, and the net EB contribution could be the sum of the contributions of Fe_3O_4 and FeO, with the second local minimum at 70 K corresponding to the T_B of FeO. Finally, above 70 K, the EB contribution is only from ferrimagnetic Fe_3O_4 , which couples to FGT through FeO. This might have weakened the exchange coupling strength, as evident from the significant training effect above 70 K (see *Figure S6* in *Section 7*).

Conclusions

In summary, we successfully demonstrated the exchange bias in $CrPS_4/Fe_3GeTe_2$ vdW heterostructures, where finite exchange bias is observed only below 36 K, the Néel temperature of $CrPS_4$. However, the introduction of a thin oxide layer at the interface affects the exchange bias significantly, and the magnitude of the exchange bias follows a complex non-monotonic trend as a function of the temperature both for field-cooling as well as for a ‘pre-set field’. The two local minima observed in the exchange bias trend with the temperature are correspond to the T_B of $CrPS_4$ and FeO. Saturating the ferrimagnetic Fe_3O_4 in the surface oxide by applying a field above a ‘critical pre-set field’ determines the direction of the unidirectional exchange anisotropy and hence the direction of loop shift. An intuitive model is proposed to explain the complex non-monotonic trend of exchange bias fields as a function of temperature. This investigation demonstrates an alternative approach to tailor exchange bias in van der Waals heterostructures by extrinsic methods such as oxidation. We believe this investigation will motivate researchers to explore the exceptional tunability of magnetic van der Waals heterostructures for spintronic applications. It would be exciting to examine how surface oxide formation on the Fe_3GeTe_2 layer affects the exchange bias due to many other vdW AFMs.

REFERENCES

- [1]. Blachowicz, T.; Ehrmann, A. Exchange bias in thin films—An update. *Coatings* **2021**, *11*, (2), 122.
- [2]. Coehoorn, R., Giant magnetoresistance and magnetic interactions in exchange-biased spin-valves. In *Handbook of Magnetic Materials*, Elsevier: 2003; Vol. 15, pp 1-197.
- [3]. Schuller, I. K.; Morales, R.; Batlle, X.; Nowak, U.; Güntherodt, G. Role of the antiferromagnetic bulk spins in exchange bias. *Journal of Magnetism and Magnetic Materials* **2016**, *416*, 2-9.
- [4]. Nogués, J.; Schuller, I. K. Exchange bias. *Journal of Magnetism and Magnetic Materials* **1999**, *192*, (2), 203-232.
- [5]. Fernando, G. W., Chapter 4 - Magnetic Anisotropy in Transition Metal Systems. In *Handbook of Metal Physics*, Fernando, G. W., Ed. Elsevier: 2008; Vol. 4, pp 89-110.
- [6]. Gong, C.; Zhang, X. Two-dimensional magnetic crystals and emergent heterostructure devices. *Science* **2019**, *363*, (6428), eaav4450.
- [7]. Phan, M.-H.; Kalappattil, V.; Jimenez, V. O.; Thi Hai Pham, Y.; Mudiyanse, N. W. Y. A. Y.; Detellem, D.; Hung, C.-M.; Chanda, A.; Eggers, T. Exchange Bias and Interface-related Effects in Two-dimensional van der Waals Magnetic Heterostructures: Open Questions and Perspectives. *Journal of Alloys and Compounds* **2023**, *937*, 168375.
- [8]. Zhu, R.; Zhang, W.; Shen, W.; Wong, P. K. J.; Wang, Q.; Liang, Q.; Tian, Z.; Zhai, Y.; Qiu, C.-w.; Wee, A. T. S. Exchange bias in van der Waals CrCl₃/Fe₃GeTe₂ heterostructures. *Nano Letters* **2020**, *20*, (7), 5030-5035.

- [9]. Dai, H.; Cheng, H.; Cai, M.; Hao, Q.; Xing, Y.; Chen, H.; Chen, X.; Wang, X.; Han, J.-B. Enhancement of the coercive field and exchange bias effect in Fe₃GeTe₂/MnPX₃ (X= S and Se) van der Waals heterostructures. *ACS Applied Materials & Interfaces* **2021**, 13, (20), 24314-24320.
- [10]. Albarakati, S.; Xie, W.-Q.; Tan, C.; Zheng, G.; Algarni, M.; Li, J.; Partridge, J.; Spencer, M. J. S.; Farrar, L.; Xiong, Y.; Tian, M.; Wang, X.; Zhao, Y.-J.; Wang, L. Electric Control of Exchange Bias Effect in FePS₃–Fe₅GeTe₂ van der Waals Heterostructures. *Nano Letters* **2022**, 22, (15), 6166-6172.
- [11]. Ying, Z.; Chen, B.; Li, C.; Wei, B.; Dai, Z.; Guo, F.; Pan, D.; Zhang, H.; Wu, D.; Wang, X.; Zhang, S.; Fei, F.; Song, F. Large Exchange Bias Effect and Coverage-Dependent Interfacial Coupling in CrI₃/MnBi₂Te₄ van der Waals Heterostructures. *Nano Letters* **2023**, 23, (3), 765-771.
- [12]. Xu, X.; Yang, S.; Wang, H.; Guzman, R.; Gao, Y.; Zhu, Y.; Peng, Y.; Zang, Z.; Xi, M.; Tian, S.; Li, Y.; Lei, H.; Luo, Z.; Yang, J.; Wang, Y.; Xia, T.; Zhou, W.; Huang, Y.; Ye, Y. Ferromagnetic-antiferromagnetic coexisting ground state and exchange bias effects in MnBi₄Te₇ and MnBi₆Te₁₀. *Nature Communications* **2022**, 13, (1), 7646.
- [13]. Peng, Y.; Ding, S.; Cheng, M.; Hu, Q.; Yang, J.; Wang, F.; Xue, M.; Liu, Z.; Lin, Z.; Avdeev, M.; Hou, Y.; Yang, W.; Zheng, Y.; Yang, J. Magnetic structure and metamagnetic transitions in the van der Waals antiferromagnet CrPS₄. *Advanced Materials* **2020**, 32, (28), 2001200.
- [14]. Wu, R.; Ross, A.; Ding, S.; Peng, Y.; He, F.; Ren, Y.; Lebrun, R.; Wu, Y.; Wang, Z.; Yang, J.; Brataas, A.; Kläui, M. Magnetotransport Study of van der Waals Cr PS₄/(Pt, Pd) Heterostructures: Spin-Flop Transition and Room-Temperature Anomalous Hall Effect. *Physical Review Applied* **2022**, 17, (6), 064038.

- [15]. Liang, J.; Liang, S.; Xie, T.; May, A. F.; Ersevrim, T.; Wang, Q.; Ahn, H.; Lee, C.; Zhang, X.; Wang, J.-P.; McGuire, M. A.; Ouyang, M.; Gong, C. Facile integration of giant exchange bias in Fe₅GeTe₂/oxide heterostructures by atomic layer deposition. *Physical Review Materials* **2023**, 7, (1), 014008.
- [16]. Gweon, H. K.; Lee, S. Y.; Kwon, H. Y.; Jeong, J.; Chang, H. J.; Kim, K.-W.; Qiu, Z. Q.; Ryu, H.; Jang, C.; Choi, J. W. Exchange bias in weakly interlayer-coupled van der Waals magnet Fe₃GeTe₂. *Nano Letters* **2021**, 21, (4), 1672-1678.
- [17]. Kim, D.; Park, S.; Lee, J.; Yoon, J.; Joo, S.; Kim, T.; Min, K.-j.; Park, S.-Y.; Kim, C.; Moon, K.-W.; Lee, C.; Hong, J.; Hwang, C. Antiferromagnetic coupling of van der Waals ferromagnetic Fe₃GeTe₂. *Nanotechnology* **2019**, 30, (24), 245701.
- [18]. Zhang, T.; Zhang, Y.; Huang, M.; Li, B.; Sun, Y.; Qu, Z.; Duan, X.; Jiang, C.; Yang, S. Tuning the Exchange Bias Effect in 2D van der Waals Ferro-/Antiferromagnetic Fe₃GeTe₂/CrOCl Heterostructures. *Advanced Science* **2022**, 9, (11), 2105483.
- [19]. Ma, S.; Li, G.; Li, Z.; Zhang, Y.; Lu, H.; Gao, Z.; Wu, J.; Long, G.; Huang, Y. 2D Magnetic Semiconductor Fe₃GeTe₂ with Few and Single Layers with a Greatly Enhanced Intrinsic Exchange Bias by Liquid-Phase Exfoliation. *ACS Nano* **2022**, 16, (11), 19439-19450.
- [20]. Ding, S.; Peng, Y.; Xue, M.; Liu, Z.; Liang, Z.; Yang, W.; Sun, Y.; Zhao, J.; Wang, C.; Liu, S.; Han, J.; Yang, J. Magnetic phase diagram of CrPS₄ and its exchange interaction in contact with NiFe. *Journal of Physics: Condensed Matter* **2020**, 32, (40), 405804.
- [21]. Och, M.; Martin, M.-B.; Dlubak, B.; Seneor, P.; Mattevi, C. Synthesis of emerging 2D layered magnetic materials. *Nanoscale* **2021**, 13, (4), 2157-2180.
- [22]. Kong, X.; Berlijn, T.; Liang, L. Thickness and Spin Dependence of Raman Modes in Magnetic Layered Fe₃GeTe₂. *Advanced Electronic Materials* **2021**, 7, (7), 2001159.

- [23]. Wu, H.; Chen, H. Probing the properties of lattice vibrations and surface electronic states in magnetic semiconductor CrPS₄. *RSC Advances* **2019**, 9, (53), 30655-30658.
- [24]. Dho, J. Magnetic-field-induced switchable exchange bias in NiFe film on (110) Fe₃O₄ with a strong uniaxial magnetic anisotropy. *Applied Physics Letters* **2015**, 106, (20), 202405.
- [25]. Radu, F.; Abrudan, R.; Radu, I.; Schmitz, D.; Zabel, H. Perpendicular exchange bias in ferrimagnetic spin valves. *Nature Communications* **2012**, 3, (1), 715.
- [26]. Koziół-Rachwał, A.; Ślęzak, T.; Nozaki, T.; Yuasa, S.; Korecki, J. Growth and magnetic properties of ultrathin epitaxial FeO films and Fe/FeO bilayers on MgO (001). *Applied Physics Letters* **2016**, 108, (4), 041606.

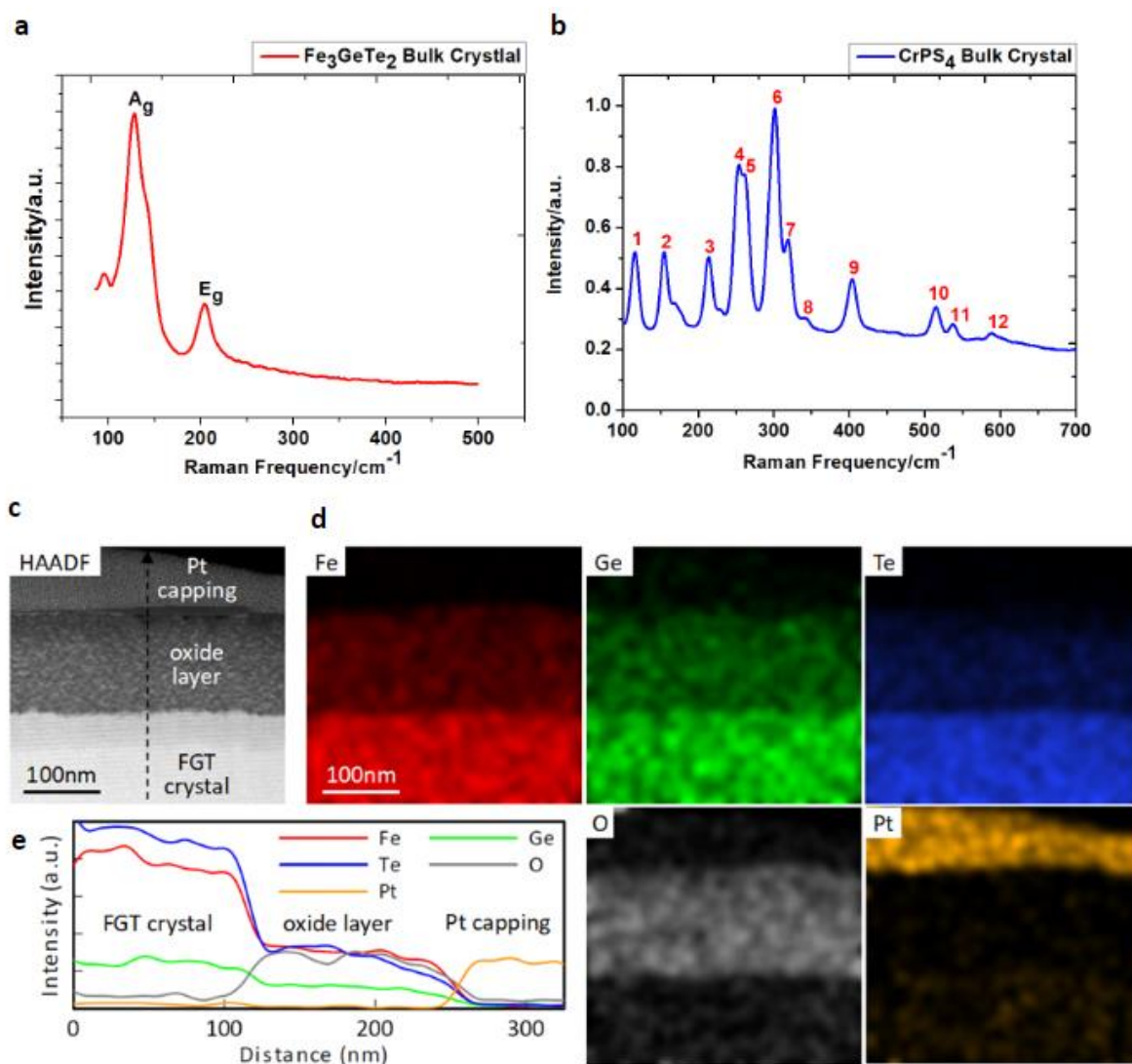


Figure 1. Structural Characterizations (a-b) Raman spectra of a FGT bulk crystal, and a CPS bulk crystal respectively. (c) Cross-sectional HAADF-STEM image of the surface region of an FGT crystal exposed to air for several days. (d) Elemental maps of Fe, Ge, Te, O and Pt obtained using EDX spectrum imaging. (e) Intensity profiles of the different elements along the vertical direction (according to the dashed arrows in (c)).

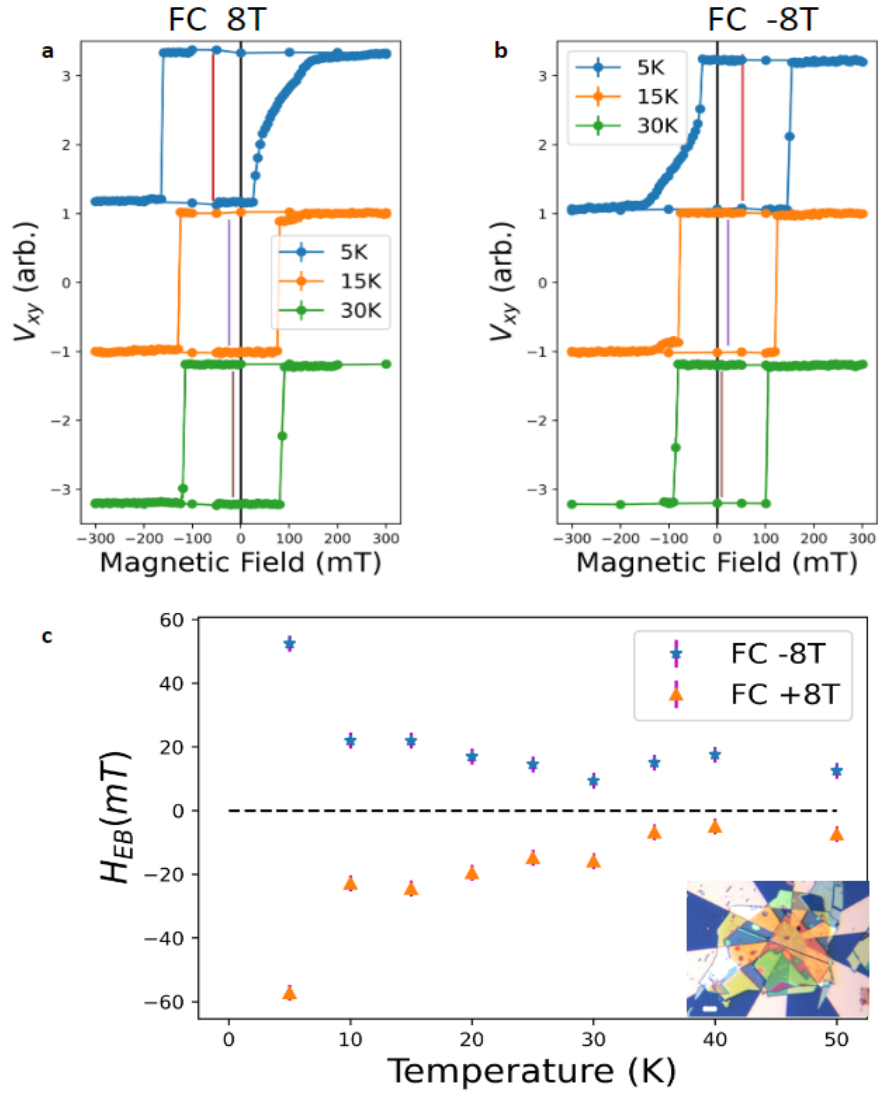


Figure 2. EB due to a clean CPS/FGT interface: EB observed for (a) +8 T field-cooling, and (b) -8 T field-cooling. (c) The trend of strength of EB as a function of temperature for both +ve and -ve 8 T field-cooling, with the optical image of the device in the inset (scale bar 10 μm).

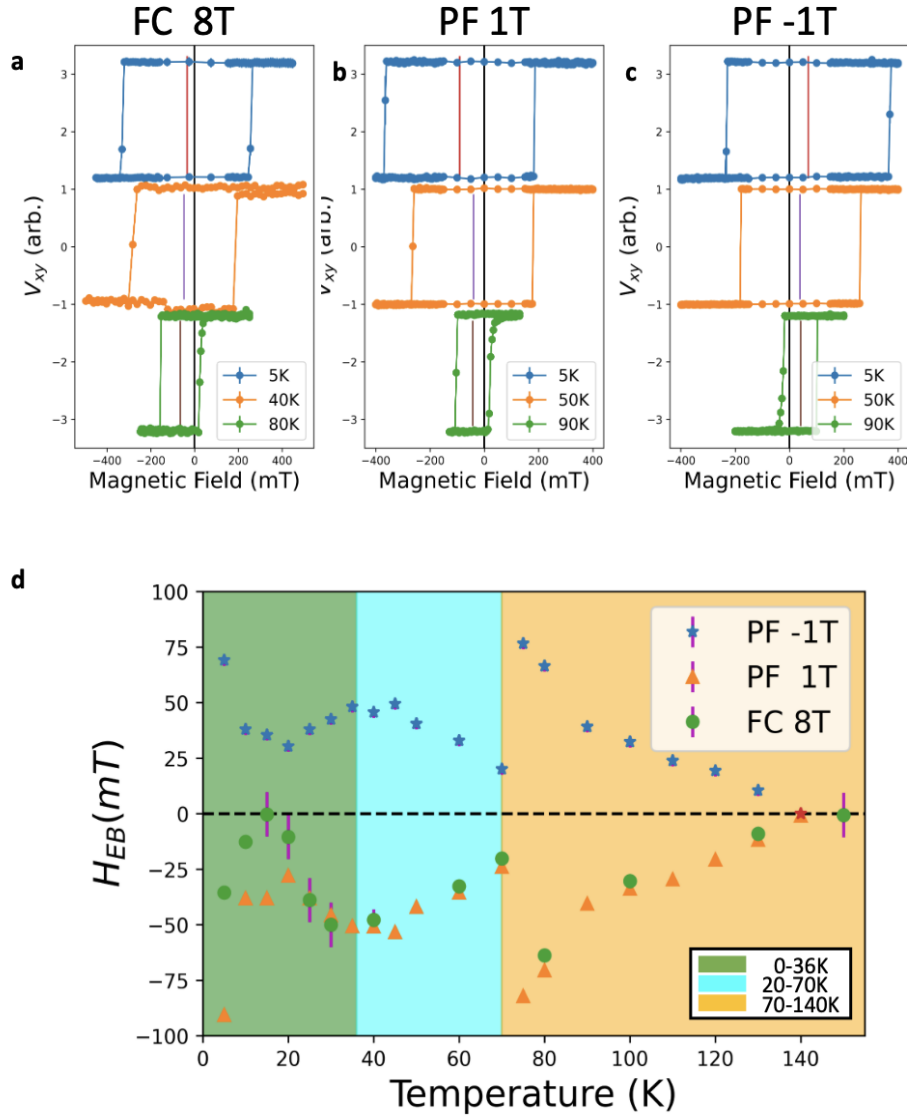


Figure 3. EB due to surface oxide layers formed at the CPS-FGT interface: EB observed for (a) +1 T pre-set field, and (b) -1 T pre-set field, and (c) +8 T field-cooling. (d) Trend of strength of EB (H_{EB}) as a function of temperature for both +ve (orange) and -ve (blue) 1 T pre-set fields as well as for the +8 T field-cooling (green).

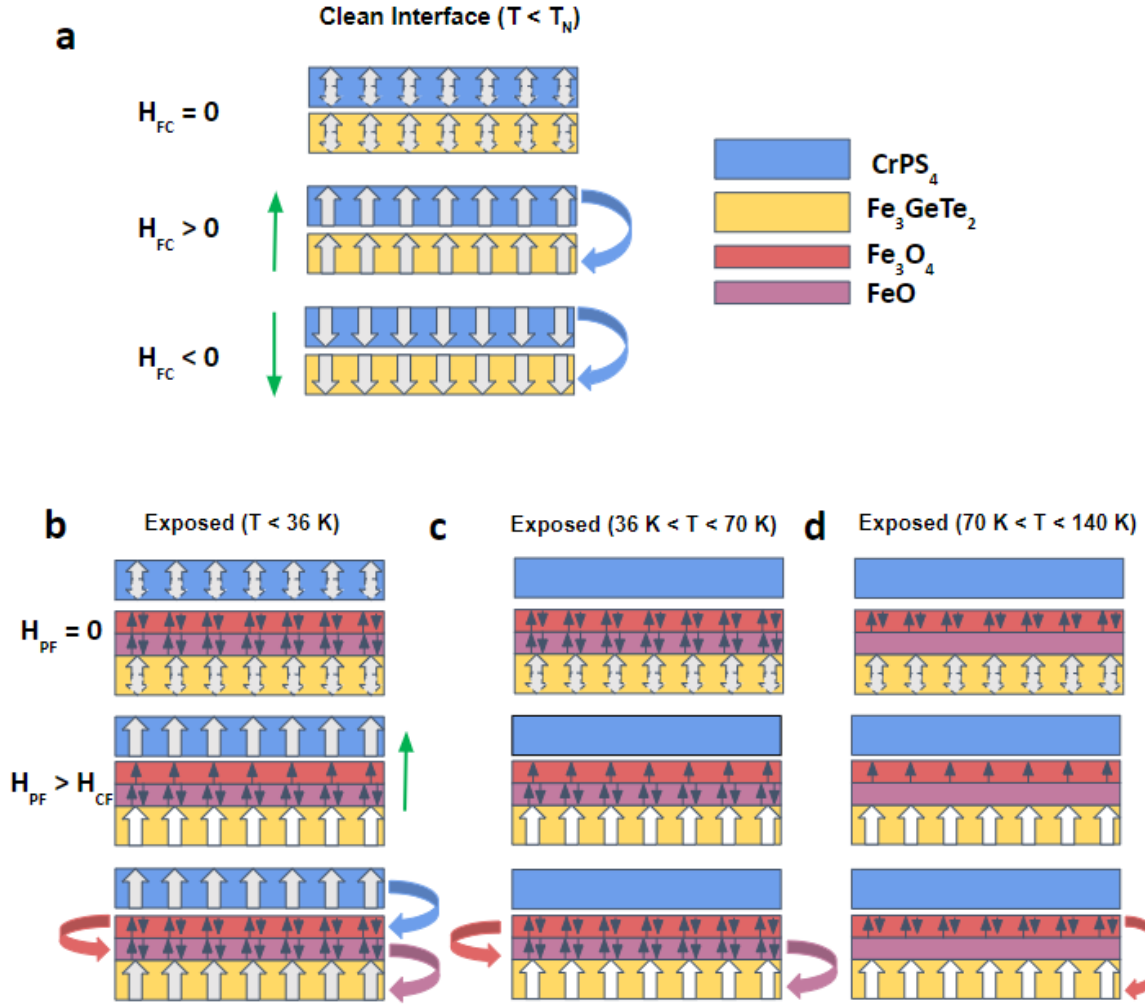
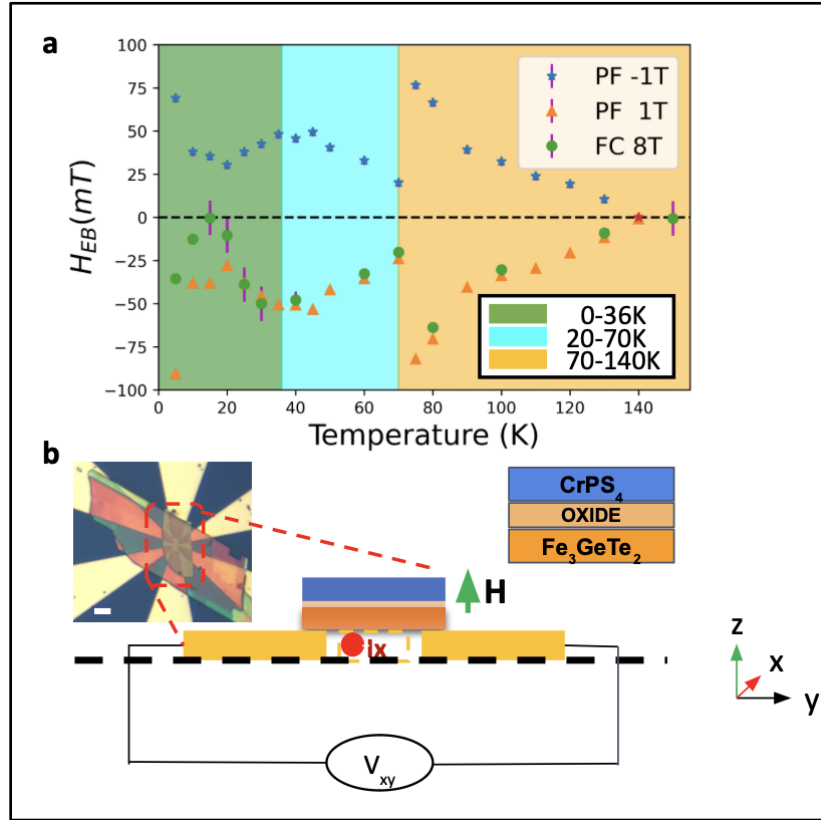


Figure 4. Schematic Model: (a) Exchange coupling in a clean interface CPS/FGT device after field-cooling (H_{FC}), and the mechanism of exchange coupling induced by a pre-set field (H_{PF}) at temperature ranges (b) $T < 36$ K (c) 36 K $< T < 70$ K and (d) > 70 K. The out-of-plane field direction is indicated by the green arrow, the exchange coupling is indicated by curved arrows, and the colour codes as indicate the respective AFM components.

SYNOPSIS



Summary of Research: (a) Unique and non-monotonic trend of the exchange bias as a function of the temperature due to the surface oxide formation on Fe_3GeTe_2 at the interface of the $\text{CrPS}_4/\text{Fe}_3\text{GeTe}_2$ AFM/FM heterostructure (b) Anomalous Hall measurement scheme with the optical image of the device in the inset (scale bar $10\ \mu\text{m}$).

Supporting Information

1. Transmission Electron Microscopy Measurement Method

Transmission electron microscopy (TEM) was carried out to confirm the oxide formation and the composition of the oxidised Fe_3GeTe_2 flake. Electron transparent cross-section view lamellas were prepared using a focused Ga^+ ion beam and scanning electron microscope (FIB-SEM) FEI Helios platform. Scanning transmission electron microscopy (STEM) and energy dispersive X-ray (EDX) spectroscopy were carried out using an FEI Titan TEM equipped with a Schottky field emission gun operated at 200 kV, a CEOS probe aberration corrector, a high angle annular dark-field detector (HAADF) and a Super-X EDX detection system. Elemental maps and profiles were obtained using the Thermo Scientific Velox software.

2. Atomic Force Microscopy

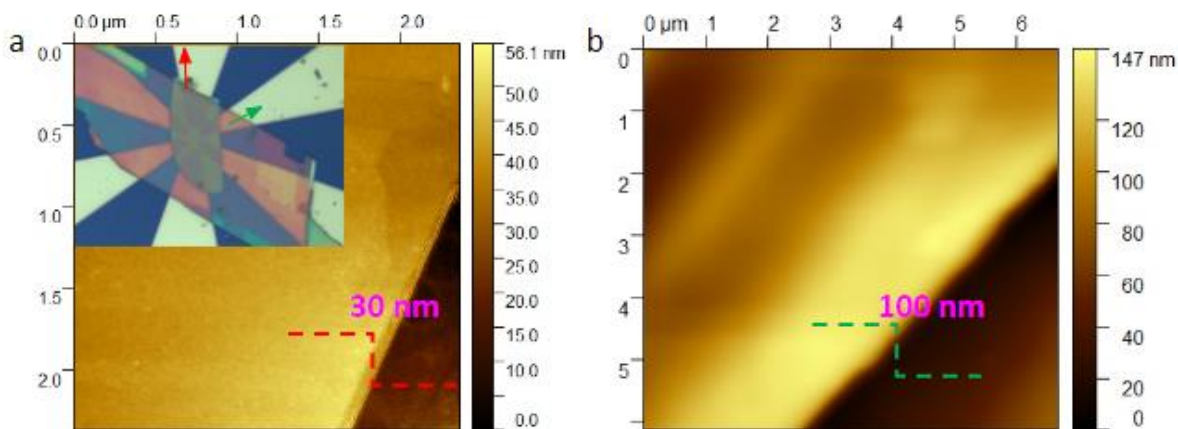


Figure S1. Atomic Force Microscope Images (a) Thickness of FGT flake, and (b) CPS flake of the exposed device. An optical image of the device is given in the inset of Figure (a) with the AFM line profiles indicated by arrows (current channel length equals 10 μm)

The thickness of the FGT and CPS of the exposed heterostructure was determined using Veeco

(Bruker) 3100 Dimension Atomic Force Microscope in tapping mode. The measurement computer is connected to a NanoScope IV controller that drives atomic force microscope and the analysis was performed using Gwyddion software. The atomic force microscope images obtained are provided in *Figure S1*. The line along which we did AFM line profile is marked in the optical image (*Figure S1a* inset) with colour coded arrows and corresponding line profile obtained a thickness of $30 \pm 2 \text{ nm}$ and $100 \pm 2 \text{ nm}$ for FGT (*Figure S1a*) and CPS (*Figure S1b*) layers respectively.

3. AHE Voltage measurements for the device with a clean CPS-FGT interface

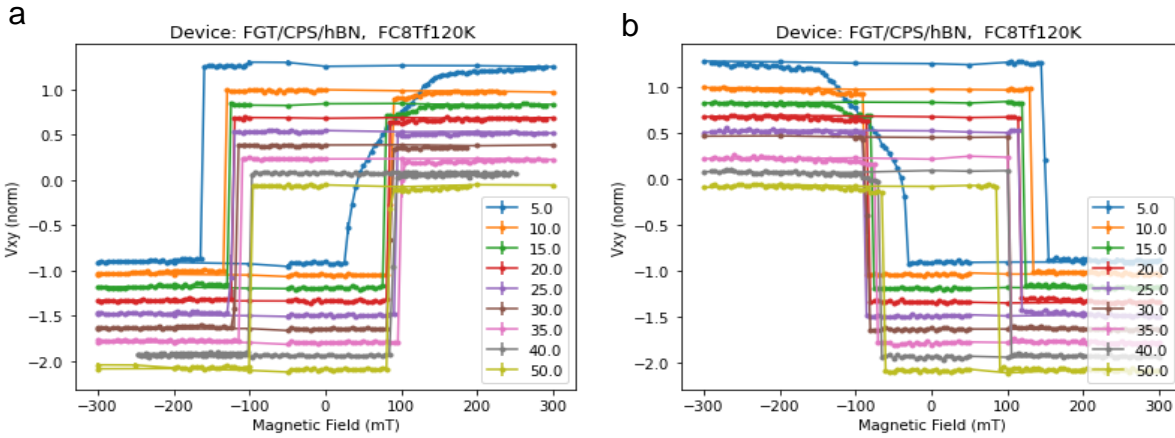
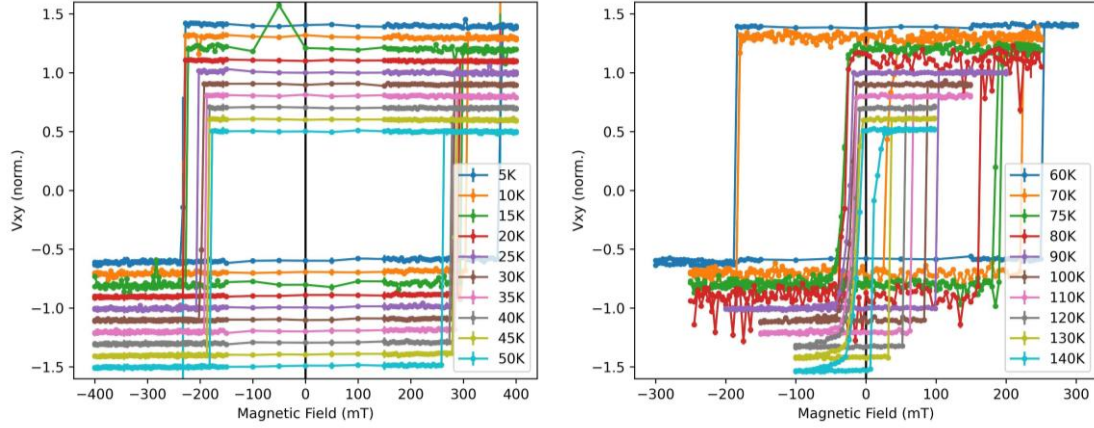


Figure S2. Out of plane magnetic field sweeps for the clean interface sample encapsulated with hBN: OOP field sweep at different temperatures from 5 K to 50 K for (a) +8 T field-cooling, and (b) -8 T field cooling. The plots are shifted along the y-axis for better legibility.

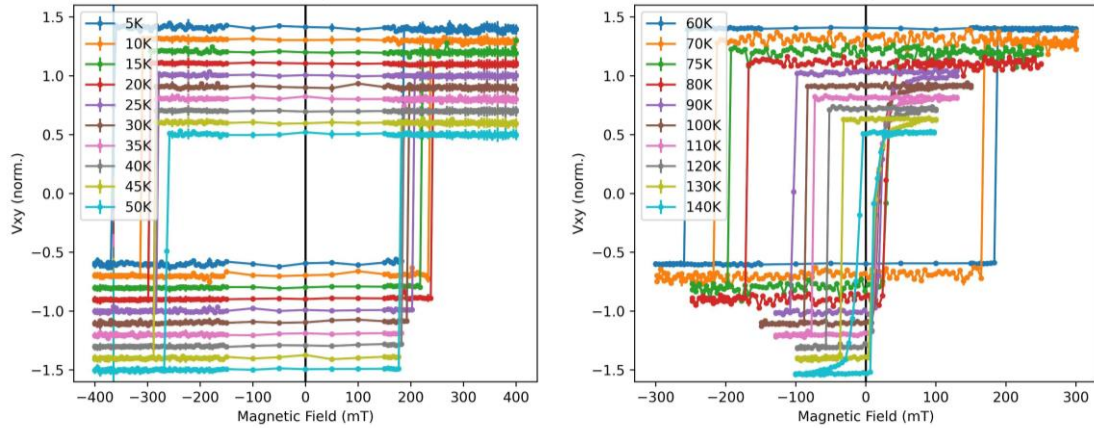
Figure S2 summarises the EB trend of the CPS/FGT heterostructure with clean interface for both +8 T (*Figure S2a*) and -8 T (*Figure S2b*) field-cooling. The magnitude of EB follows similar trend with respect to the temperature for both +8 T and -8 T field cooling with a maximum of $|H_{EB}| \sim 55 \text{ mT}$ at 5 K and gradually decreases to $< 20 \text{ mT}$ above 20 K. The FM hysteresis plots become symmetric above 36 K, the Néel temperature of CPS.

4. AHE Voltage measurements for the device with additional oxide layer at the CPS-FGT interface

a



b



c

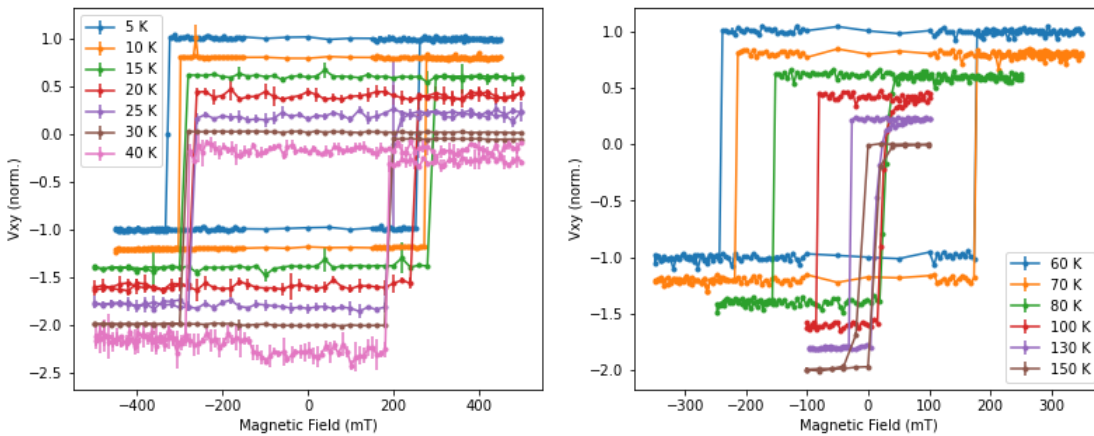


Figure S3. OOP plane magnetic field sweeps for the sample with Fe_3GeTe_2 surface oxide at the interface (FGT/OFGT/CrPS₄): OOP field sweep at different temperatures from 5 K to 140 K for (a) -1 T pre-set field, and (b) +1 T pre-set field, and (c) +8 T Field-cooling. The plots are shifted along the y-axis for better legibility.

Figure S3 describes the EB observed for an exposed CPS/FGT heterostructure having an additional oxide layer at the interface. The additional oxide layer introduced at the interface enables the heterostructure to have EB above the Néel temperature of CPS (36 K) and EB is observed up to 140 K. Additionally, the oxide layer is capable of inducing EB even without a field-cooling. We observed EB of comparable magnitude and direction to that of field-cooling just by applying a pre-set field (H_{PF}) of ± 1 T before the field sweep. The anomalous hall voltage measured as a function of applied field for different temperatures from 5 K to 140K for $H_{PF} = -1$ T (Figure S3a), $H_{PF} = +1$ T (Figure S3b), and for a +8T field-cooling (Figure S3c) are summarised in Figure S3.

5. Transport across a possible Verwey transition

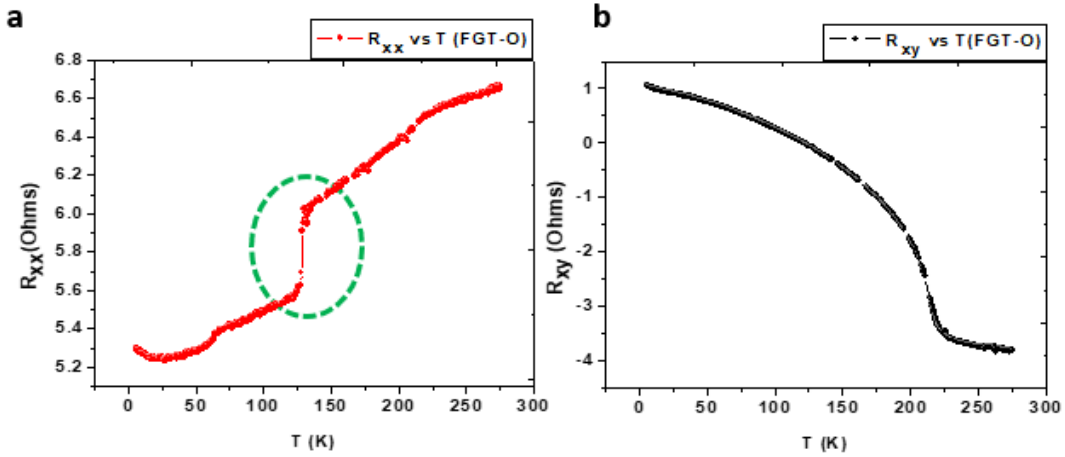


Figure S4. Transport across Verwey transition: (a) Longitudinal resistance (R_{xx}) as a function of temperature (at $\mu_0 H = 0.1$ T) highlighting (green dotted ellipse) a sudden rise characteristic of insulator to half-metallic Verwey transition in Fe_3O_4 , whereas (b) the transverse Hall resistance (R_{xy}) as a function of temperature (at $\mu_0 H = 0.1$ T) is unaffected since the ultra-thin oxide contribution could be subtle compared to bulk FGT.

Figure S4 summarises the longitudinal (R_{xx}) and transverse Hall resistance (R_{xy}) of an oxidized FGT flake. As we know, an Fe_3O_4 layer might be having a magneto-structural phase transition about 80 K to 125 K which is known as Verwey transition (T_V). At this point, magnetite undergoes a phase transition from insulating monoclinic structure to a half-metallic inverse spinel cubic structure [1]. Here, R_{xx} (Figure S4a) has a sudden rise at around 125 K could be corresponding to the Verwey transition (T_V) of the magnetite oxide layer. Below T_V , since the magnetite layer is in insulating monoclinic phase, the current flows only through FGT. However, above T_V current can flow through both FGT as well as the Fe_3O_4 layer as indicated by a sudden rise in R_{xx} at $T_V = 125 \text{ K}$. However, the oxide layer seems to have little effect on Hall (transverse) resistance (Figure S4b).

6. Influence of ferrimagnetic Fe_3O_4 on exchange bias

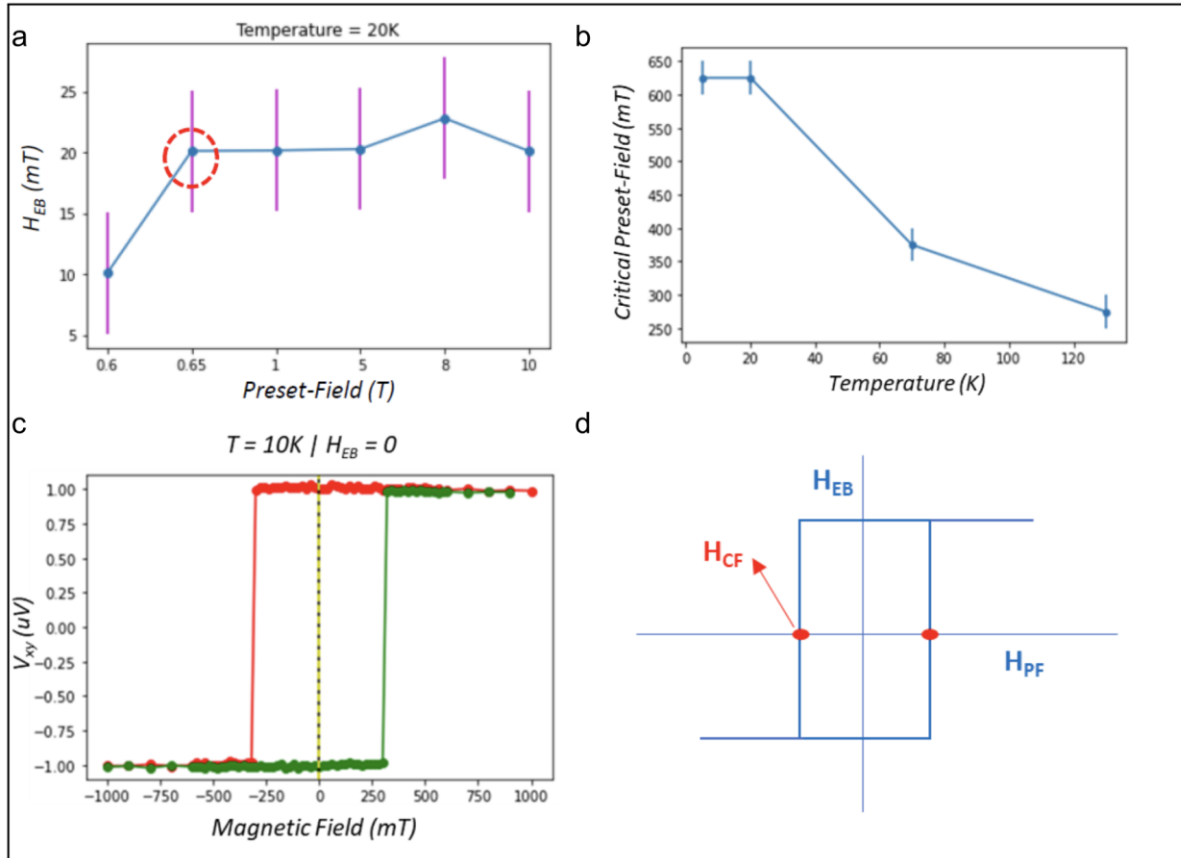


Figure S5. Influence of Ferrimagnetic Fe₃O₄ Oxide (a) The critical pre-set field (H_{CF}) determined at $T = 20$ K. (b) The variation of magnitude of H_{CF} against temperature. (c) At 10 K, a sweep with a maximum field value (1 T) greater than H_{CF} (~ 600 mT) results in vanishing of EB. (d) Schematic representation of how exchange bias evolves with a pre-set field with the critical points marked with red dots.

Figure S5 explains how a ferrimagnetic Fe₃O₄ layer generates a pre-set field (H_{PF}) induced EB. H_{EB} was determined for different values of H_{PF} and plotted as a function of H_{PF} (*Figure S5a*). We observed that H_{EB} remains constant beyond a critical value of H_{PF} , which is termed as critical pre-set field (H_{CF}) and the magnitude of H_{CF} found to be decreasing as we increase the temperature (*Figure S5b*). Such a variation of H_{CF} as a function of temperature is similar to how the coercive field of a ferrimagnetic Fe₃O₄ varies with temperature. Moreover, after applying a $H_{PF} = \pm 1$ T, if we sweep the field with a maximum field greater than the H_{CF} at a particular temperature, the EB vanishes since there is no preferred orientation for the ferrimagnetic Fe₃O₄ that sets the EB. In *Figure S5c*, the AHE voltage (V_{xy}) as a function of sweeping field at 20 K after applying $H_{PF} = +1$ T shows a symmetric hysteresis since the maximum sweeping field in positive and negative direction (± 1 T) is greater than the H_{CF} of the Fe₃O₄ layer at 20 K ($H_{CF} \sim 0.65$ T). Importantly, at a given temperature, we could choose the direction of the EB just by saturating the ferrimagnetic Fe₃O₄ along a preferred direction by applying a $H_{PF} > H_{CF}$, which is schematically demonstrated in *Figure S5d* – a plot showing how the EB (H_{EB}) varies as a function of H_{PF} .

7. Strength of exchange bias below and above 70K

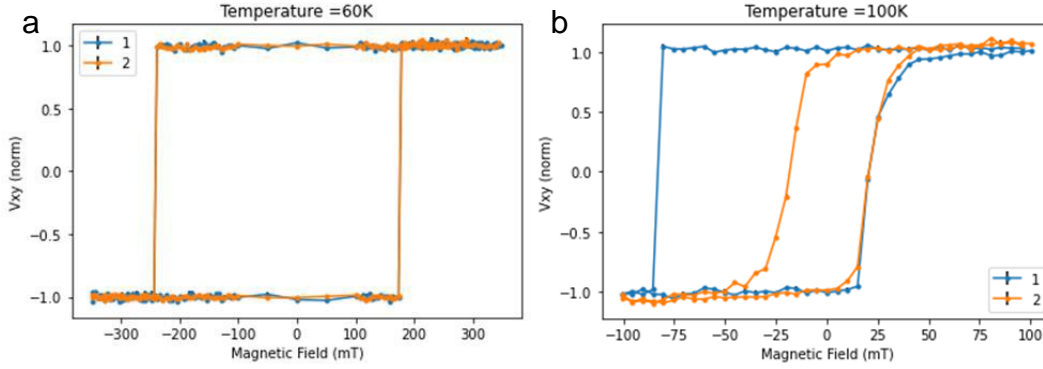


Figure S6. Training effects below and above 70 K: The exchange bias below 70 K is immune to training effect however above 70 K it seems to diminish drastically after the first cycle. The FeO at the interface below 70 K is antiferromagnetic and hosts exchange bias through it whereas it acts like a spacer layer above 70 K.

Finally, *Figure S6* shows little (*Figure S6a*) and significant (*Figure S6b*) training effect for two consecutive field sweeps measured after a $H_{PF} = +1$ T for the device with additional oxide layer at the interface. It gives a measure of the strength of EB on either side of the minimum at $T = 70$ K in the plot showing variation of H_{EB} as a function of temperature (Please refer main *Figure 3d*). 70 K is the blocking temperature of the antiferromagnetic FeO above which it does not contribute to EB and act as a spacer layer between FGT and top Fe_3O_4 layer in the surface oxide (please refer to the intuitive model provided in *Figure 4d*). Such a spacer layer might be responsible for a significant training effect above 70 K. Moreover, the observed asymmetry in the loop behaviour above 70 K is attributed to the difference in effective fields experienced by FM spins from the ferrimagnetic sub-lattices while rotating through the forward and reverse direction [2].

References

- [1] Piekarz, Przemysław, Krzysztof Parlinski, and Andrzej M. Oleś. "Mechanism of the Verwey transition in magnetite." *Physical Review Letters* 97.15 (2006): 156402.
- [2] Stamps, R. L. "Mechanisms for exchange bias." *Journal of Physics D: Applied Physics* 33.23 (2000): R247